NASA CONTRACTOR REPORT 182018

DELAMINATION FAILURE IN A UNIDIRECTIONAL CURVED COMPOSITE LAMINATE

RODERICK H. MARTIN

Analytical Services and Materials, Inc.
Hampton, Virginia

Contract NASI-18599
APRIL 1990

National Aeronautics and
Space Administration

Langley Research Center
Hampton, Virginia 23665-5225

ABSTRACT

This paper investigated delamination failure in a unidirectional curved composite laminate. The curved laminate failed unstably by delaminations developing around the curved region of the laminate at different depths through the thickness until virtually all bending stiffness was lost. Delamination was assumed to initiate at the location of the highest radial stress in the curved region. A closed form curved beam elasticity solution and a 2-D finite element analysis (FEA) were conducted to determine this location. The variation in the strain energy release rate, G, with delamination growth was then determined using the FEA. A strength-based failure criterion adequately predicted the interlaminar tension failure which caused initial delamination onset. Using the G analysis the delamination was predicted to extend into the arm and leg of the laminate, predominantly in mode I. As the initial delamination grew around the curved region, the maximum radial stress in the newly formed inner sublaminate increased to a level sufficient to cause a new delamination to initiate in the sublaminate with no increase in applied load. This failure progression was observed experimentally.

INTRODUCTION

With the increased use of laminated fiber reinforced composite materials in primary aircraft structural components, the ability to understand and predict their failure modes becomes paramount. Because of the low through-the-thickness strengths of composites one of their prime modes of failure has been delamination [1]. The high interlaminar stresses which may cause delamination can arise from material discontinuities, geometric

discontinuities, or eccentricities in the load path. One example of a generic structural component which has the possibility of all three of these interlaminar stress sources is the curved laminate. Some typical uses of a curved composite laminate are shown in fig. 1. Mostly, the laminates are of a multidirectional layup. The material property mismatch between adjacent plies of different orientation may create singular interlaminar stresses at the free edge causing edge delamination [2]. Another failure mode occurs when the membrane stresses in off-axis plies are high and cause transverse tension cracking across the width [3]. Mathematically singular interlaminar stresses may occur where the matrix crack meets the adjacent plies. These stresses may cause delamination at this location. Delamination may also occur as an interlaminar tension failure caused by tensile radial stresses created from the bending of the curved laminate.

Several studies in the literature have focused on determining damage in curved laminates. In reference 4, a finite element analysis was used to determine the strain distribution for the design of curved composite frames for the UH60 Black Hawk Helicoptor. In reference 5, a strength-based criterion based on the Tsai-Hill criterion was used to predict if an off-axis ply failure or an interlaminar tension failure would occur in multidirectional curved laminates. In reference 6, a finite element analysis and a closed-form solution was conducted to determine the stress distribution in a curved composite frame taken from the V22 Osprey. The Tensor Polynomial criterion was used to predict failure. In reference 7, an elasticity solution was used to determine the stress distribution in a semi-circular composite beam. In reference 8, composite angles of different lay-ups were tested and analysed. Different failure modes were noted. In one lay-up the failure was delamination from an interlaminar tension failure and in another failure was matrix cracking in a 90^0 ply followed by delamination initiating from the

matrix crack. A strength-based failure criteria predicted the different failure modes but yielded generally conservative predictions.

A review of some of the work conducted on curved composite beams and frames was given in reference 9. Reference 9 notes that predicting delamination is difficult to do using strength-based failure criteria because adequate test methods for determining the through-the-thickness strengths, σ_{3f} and τ_{13f}, do not exist. A further problem with the use of strength-based criteria in the above examples is in the determination of the stresses. Although a stress analysis may be useful to identify the areas that are highly stressed, a strength-based failure criteria may only be used when no singular stresses are present. As soon as some damage or other discontinuity is present, such as a radial delamination, a matrix crack, or a free edge, stresses cannot be evaluated at the singularities, and a strength criteria should not be used. Fracture mechanics based failure criteria offer a technique to predict the strength and life of a component with a singularity caused by a discontinuity. An attempt to use a fracture mechanics approach to predict the static strength of a curved laminate containing both a matrix crack and a radial delamination was given in reference 10. The failure loads predicted were generally unconservative, possibly because the 2-D finite element analysis did not account for the effects of the free edge. In reference 11, delamination was assumed to exist in a production part in a curved solid laminate segment of a fuel sponson. The failure was assumed to occur during manufacture due to residual thermal stresses. A 2-D coupled boundary element fracture mechanics approach was used to determine how large the delamination could become before the component failed for a given design load. It was determined that long before total failure of the component the delamination could be easily detected by NDI methods. A fracture mechanics based methodology for predicting the static strength and the fatigue life of

other structural components which experience delamination initiating from singular stress sources has been proposed [12-15]. This methodology uses analyses to determine the critical value of strain energy release rate, G , and its components along with delamination onset data obtained from generic test coupons [16-20].

The purpose of this paper is to predict the maximum load a unidirectional curved laminate can sustain. Unidirectional laminates were used to isolate the interlaminar tension failure, that is it was insured that no edge delamination or delamination from cracked plies would occur. Simple right-angled coupons were analysed and tested to represent the loading on the angle bracket configuration shown in fig. 1. First, the location of initial failure was determined using a stress analysis assuming an undamaged component containing no singular stress sources. A closed form curved beam elasticity solution and a finite element analysis (FEA) were used to compute the interlaminar stresses. Secondly, a fracture mechanics analysis was conducted to determine damage progression after the onset of delamination. This characterization was done by determining how G varies with delamination growth. A methodology for computing the variation of G for an embedded delamination with two delamination fronts was developed. Further damage progression was then determined by analyzing the curved laminate with the delamination present.

NOMENCLATURE

a	Delamination length in the counter-clockwise direction
b	Delamination length in the clockwise direction
c, R_{inner}	Inner radius
d	Outer radius
E_r, E_{22}, E_{33}	Radial/transverse tensile moduli
E_θ, E_{11}	Tangential/longitudinal tensile moduli
F_r	Force in the radial direction
F_θ	Force in the tangential direction

FAW	Fiber areal weight
FD	Fiber density
G_{Ic}	Critical value of mode I strain energy release rate
G^{SE}	Total strain energy release rate calculated from change in strain energy
G^{VT}	Total strain energy release rate calculated from virtual crack closure technique (VCCT)
G_I^{VT}	Mode I strain energy release rate calculated from VCCT
G_{II}^{VT}	Mode II strain energy release rate calculated from VCCT
$G_{r\theta}, G_{12}, G_{13}$	Transverse shear modulus
h	Ply thickness
l	Total delamination length
L, L_1	Length of moment arm
M	Moment
N	Number of plies
P	End load
r	Radius
R	Radial distance of delamination onset
t	Thickness of specimen
V_f	Volume fraction
w	Width of beam
α	Angle of delamination in counter-clockwise direction
β	Angle of delamination in clockwise direction
δ_r	Displacement in the radial direction
δ_θ	Displacement in the tangential direction
θ	Angle around curved region from leg
κ	Anisotropic parameter for moments
λ	Length of finite element at delamination front
$\nu_{r\theta}, \nu_{21}$	Poisson's ratio
σ_{2f}, σ_{3f}	Transverse tensile strengths
σ_r	Radial stress
σ_r^M	Radial stress caused by moments
σ_r^P	Radial stress caused by end loads
σ_θ	Tangential stress
σ_θ^M	Tangential stress caused by moments
σ_θ^P	Tangential stress caused by end loads
τ_{12f}, τ_{13f}	Shear strengths
$\tau_{r\theta}$	r-θ shear stress
$\tau_{r\theta}^M$	r-θ shear stress caused by moments
$\tau_{r\theta}^P$	r-θ shear stress caused by end loads
ϕ	Total angle of delamination = $\alpha + \beta$
ω	Anisotropic parameter for end loads

MATERIALS

Twenty-four ply, graphite/epoxy (AS4/3501-6) unidirectional curved laminates were manufactured at NASA Langley Research Center. The laminates were cured according to the manufacturer's instructions. The curved laminates were layed up over a solid aluminum tool in panels 300 mm wide to give a 90° bend. Following curing, the panels were cut into 25 mm wide specimens. The final dimensions of the curved laminates are given in figure 2. Double Cantilever Beam, DCB, specimens were also manufactured. The DCB specimens were 24-ply unidirectional coupons with a sheet of 0.127 mm (0.5mil) Kapton film placed between the 12th and 13th plies prior to curing to simulate a delamination. The dimensions of the DCB specimens were given in reference 17. The following values of fracture toughness were obtained from delamination growth initiating at the insert:

$$69.0 \leq G_{Ic} \leq 99.0 \text{ J/m}^2 \quad (\text{mean} = 80.0 \text{ J/m}^2)$$

Values for transverse tensile strength obtained from flat specimens were taken from reference 21 and were:

$$36.5 \leq \sigma_{2f} \leq 69.0 \text{ MPa} \qquad (\text{mean} = 53.8 \text{ MPa})$$

Specimens to determine the elastic properties of the composite were also manufactured. The elastic tensile and shear properties used in the FEA and the closed form elasticity solution were obtained using ASTM standards D3039 and D3518, respectively. The following average properties from at least three tests were obtained assuming transverse isotropy:

$$E_{11} = E_{\theta} = 138 \text{ GPa} \qquad E_{22} = E_{33} = E_r = 10.0 \text{ GPa}$$

$$G_{12} = G_{r\theta} = 4.47 \text{ GPa} \qquad \nu_{12} = \nu_{13} = 0.3 \qquad \nu_{21} = \nu_{31} = \nu_{r\theta} = 0.0218$$

The average volume fraction, V_f, of the specimens was determined from $V_f = \frac{FAW \times N \times 100}{FD \times t}$ where FAW is the fiber areal weight, N is the number of plies, FD is the fiber density, and t is the thickness of the specimen. For the DCB specimen, V_f was determined to be 55.9 percent. In the curved laminate specimens, V_f in the curved region was 54.7 percent and in the leg V_f was 56.1 percent. In the specimens used to obtain elastic moduli, V_f = 59.1 percent.

EXPERIMENTAL PROCEDURE AND RESULTS

A special fixture for testing the curved laminates in a standard tensile testing machine was manufactured and is shown in fig. 3. A 890 N (200 lb) load cell was incorporated into the test fixture to monitor accurately the small loads associated with matrix failures in composites. The load was applied to the specimen at a distance L of 50 mm from the curved region/arm intersection via a hinge clamped to the specimen. The other end of the hinge was held in a clamp that was free to pivot. The displacements were small during the test because of the high stiffness of the unidirectional curved laminate. Therefore, the load applied via the hinge was considered to remain vertical during testing. A displacement transducer, not shown in fig. 3, was attached to the side of the loading arrangement to measure vertical displacements during the tests. The edges of the specimens were painted with a brittle white paint to aid visualization of interlaminar failures. The load and displacement were monitored on an X-Y plotter to determine the failure load. The laminates were loaded quasi-statically in load control.

The maximum static loads per unit width for damage initiation in the unidirectional curved laminates are shown in table 1. A significant scatter can be seen in the results. A similar scatter was reported in reference 6 and

is consistent with the large scatter in transverse tensile strength in reference 21. The specimens were labeled sequentially from the location they were cut from the panels. There was no trend found between the strength and the location where the curved laminate was cut from the panel. The normalized radius location of the first delamination is also given in table 1. The damage in three different specimens is shown in fig. 5. Damage initiated, fig. 5a, as a single delamination around the curved region. Growth was initially unstable and extended into the arm and the leg. Two delaminations around the curved region are shown in fig. 5b. the lower delamination is at an $(R-R_{inner})/t$ of 0.23. Final damage was an accumulation of delaminations at different locations in the thickness of the curved region until the specimen lost virtually all bending stiffness. The longest delamination in fig. 5c is at an $(R-R_{inner})/t$ of 0.46 and was presumably the first delamination to occur. For the upper two photographs shown in fig. 5 to be taken, the load was reduced manually when audible accoustic emissions were heard.

ANALYSIS

The following section details the analysis required to characterize the onset and growth of a delamination in the unidirectional curved laminate. The location of the highest radial stress, σ_r to cause delamination was determined using a closed form elasticity solution for an anisotropic curved beam. A 2-D FEA was conducted to verify the beam solution and determine the variation of G with delamination growth from the location of highest radial stress.

Closed Form Anisotropic Elasticity Solution for a Curved Beam

The loading on the curved laminate used in the experimental work may be reduced to a curved beam with an end load, P, and moment, M, at the free end

of a quarter of a curved circular beam, figure 4. The stresses created in the beam may be calculated by summing the stresses caused by the end load and the moment. A closed form elasticity solution for the stresses in a curved beam with cylindrical anisotropy and subjected to end forces and moments was given in reference 22 and is repeated in Appendix A using the notation give in fig. 6. It was assumed that the location of the maximum radial stress in the curved portion may indicate where delamination onset will occur. The maximum radial stress was determined by solving

$$\frac{d\left[\sigma_r^P + \sigma_r^M\right]}{dr} = 0 \qquad (1)$$

$$\frac{d\left[\sigma_r^P + \sigma_r^M\right]}{d\theta} = 0 \qquad (2)$$

for R and θ, where σ_r^P is the radial stress created by the end load P and σ_r^M is the radial stress created by the moment M. The solution yielded a maximum value of $\left[\sigma_r^P + \sigma_r^M\right]$ at R= 6.21 mm and θ=0°. This value of R was approximated to R=6.25 mm which was the closest radius to two ply interfaces. However, the boundary conditions are for a curved beam and not a laminate with straight attachments. To determine the effect of straight legs attached to a quarter circle a finite element analysis, described in the next section, was conducted.

Finite Element Analysis

A 2-D FEA was conducted using the finite element code NASTRAN [23] using two different models. Model 1, shown in fig. 7a, was used to determine the stresses in the curved region of the beam assuming no damage in the part. The model had one element per ply thickness and one element per one degree sweep

around the curved region. The model had a unit end load per width (1.0 N/mm) applied at a length of 50 mm along the arm to simulate the experimental conditions. Model 2 with a refined mesh, fig. 7b, was used so that the virtual crack closure technique, VCCT, [24] could be employed to determine total G and its components corresponding to delamination growth. The mesh was refined at R=6.25 mm which was the radius determined from the closed form elasticity solution (and the FEA as described later) where delamination was expected to initiate. Near a radius of R=6.25 mm the finite elements measured h/4 by h/4.6 where h is one ply thickness. At a radius of R=6.25 mm a free surface was included in the model by the use of coincident nodes to represent the delamination. The free surface extended around the complete 90^0 of the curved region. The coincident nodes were restrained together using multi-point constraints (MPCs). By releasing different MPCs in different analysis cases, several delamination lengths could be modeled during one FEA run yielding an efficient computational technique. To reduce the number of elements in the model the length of the arm was shortened to L_1=5 mm. A load and moment were applied to the shortened arm, fig. 4. The load and moment were equivalent to an end load of 1 N/mm applied at a moment arm length of 50 mm.

Calculation of Strain Energy Release Rate

The virtual crack closure technique was used to obtain total and individual modal values of G at the delamination fronts. The individual modes of G were calculated at the delamination front using the following equations in polar coordinate notation, fig.8,

$$G_I^{VT} = \frac{1}{2 \lambda w} F_r^A \left(\delta_r^B - \delta_r^C \right) \qquad (3)$$

$$G_{II}^{VT} = \frac{1}{2 \lambda w} F_{\theta}^{A} \left(\delta_{\theta}^{B} - \delta_{\theta}^{C} \right) \quad (4)$$

where F_r^A and F_θ^A are the radial and tangential forces at node A respectively, λ is the length of the finite element at the delamination front, δ_r and δ_θ are the radial and tangential displacements at the nodes indicated by the superscripts, and w is the width of the model. Total G calculated by VCCT, G^{VT}, was simply a summation of G_I^{VT} and G_{II}^{VT}.

An alternative method of calculating total G to check the VCCT results was also used. This method involved determining the difference in total strain energy from two finite element runs at two delamination lengths, l_i and l_{i+1}, thus

$$G^{SE} = \frac{1}{2 w (l_i - l_{i+1})} \left[\Sigma (P \delta)_{l_i} - \Sigma (P \delta)_{l_{i+1}} \right] \quad (5)$$

where $\Sigma(P \delta)$ is the sum of the product of the applied loads and the displacements (in the loading direction) of the loaded nodes. The resulting G^{SE} approximately applies at a delamination length of $(l_i + l_{i+1})/2$.

ANALYTICAL RESULTS

Stress Distribution

Figures 9 and 10 show the radial, transverse shear and tangential stresses, respectively, as calculated by the closed form elasticity solution and FEA. The stresses were normalized by P/w. The stresses are plotted versus the normalized radius at an angle $\theta = 25^0$. The choice of this angle will become apparent in the next paragraph. In fig. 9 the agreement for the radial and transverse shear stress between the two analytical methods was good and confirms that the radial stress was highest at $(R-R_{inner})/t = 0.42$

(R≈6.25 mm). The transverse shear stress was approximately an order of magnitude smaller than the radial stress. The agreement in fig. 10 was also good and shows that the laminate has a maximum tensile tangential stress at the inside edge of the curved region.

Figure 11 shows the normalized radial stress plotted around the radius at R=6.25 mm. The closed form elasticity solution agreed well with the FEA for $20^0 \leq \theta \leq 60^0$. However, as θ approaches the boundaries the two solutions diverge as expected from St. Venant's principle. According to the FEA the radial stress reaches a maximum at $\theta=25^0$. Therefore, the location for the onset of delamination was determined from figures 9-11 to be at R=6.25 mm at an angle $\theta = 25^0$.

Strain Energy Release Rate Variation with Delamination Growth

Next, the variation of G with delamination growth was determined. The delamination had two fronts which may have different values of G. Referring to fig. 6, the delamination front may grow counter-clockwise or clockwise from the initiation point (R=6.25 mm, $\theta=25^0$) as indicated by the letter a or b, respectively. The delamination length is given by a+b where $a = \frac{2 \pi R \alpha}{360}$ and $b = \frac{2 \pi R \beta}{360}$ and α and β are measured in degrees.

Figure 12 shows the normalized G distribution ($G w^2/P^2$) with delamination growth in the α direction only, that is holding β equal to zero. The delamination was predominantly mode I around the curved region. The normalized values of G^{VT} obtained by VCCT ($G_I^{VT} + G_{II}^{VT}$) closely agree with values obtained using the change in global strain energy technique, G^{SE}. Both G^{SE} and G_I^{VT} increase to a maximum at $\alpha=22^0$ and then reduce. At $\alpha=25^0$ the delamination is at the curved region/leg boundary.

Figure 13 shows the normalized G distribution in the β direction, holding α equal to zero. Again the delamination growth was predominantly mode I around the curved region. The total G results from VCCT and the change in global strain energy technique again agree well. Both G_I^{VT} and G^{SE} increase from zero to a maximum and then decrease. For G_I^{VT} the maximum is at β=48° while for G^{SE} the maximum is at β=50°. The difference between the two peaks is caused by the increase in G_{II}^{VT}. Fig. 13 shows that G_{II}^{VT} increases throughout the curved portion of the beam. However, as the delamination grows into the arm, the horizontal forces caused by the moment would decrease. Hence, G_{II}^{VT} should reach a maximum at the start of the arm, and decrease as the delamination grows into the arm.

Figures 12 and 13 show how G varies when either one of the two fronts grows individually. However, they do not show how the two fronts grow simultaneously. Consider an angle ϕ, where $\phi=\alpha+\beta$. Also, assume that the delamination grows equally in the a and b direction, hence, $\alpha=\beta=\frac{\phi}{2}$. The result of assuming this delamination growth behavior is given in fig. 14. Note that when ϕ=50°, the delamination has grown fully around the curved region to the leg but has not yet reached the arm, fig. 6. For small angles of ϕ, G_a and G_b are similar and the delamination should grow equally in the α and β direction. However, at larger angles of ϕ, G_a becomes less than G_b because σ_r is decreasing more rapidly in the α direction than in the β direction, fig. 11. Hence, the delamination would continue to grow in the β direction and not in the α direction. Thus, any subsequent data points in fig. 14 are invalid. Delamination growth must be represented incrementally

and G_a and G_b compared at each increment. If G at one end of the delamination is higher than that at the other, then the delamination will grow in that direction only. Following that incremental growth another analysis must be conducted, and so on until the delamination arrests or failure occurs. Hence, a methodology was developed to ensure a constant G existed at both delamination fronts. A criterion was employed that if G was two percent greater at one delamination front than at the other, then growth would occur in that direction only. If the difference was less than two percent then the delamination would grow in both directions simultaneously. For the first increment a 5^0 step was taken from the initiation site. From there, incremental delamination growth steps of 2.5^0 or 0.273 mm were assumed. The results are shown in fig.15. Note that G_a is plotted against α which ranges from 0 to 25^0 whereas G_b is plotted against β, which ranges from 0 to 65^0. From the onset location, the delamination grows simultaneously in both directions as indicated in figure 14. However, at the third increment G_b was 3.7 percent higher than G_a. Hence, delamination growth was assumed to occur in the β direction alone, and is shown in fig. 15 by the next G_a value being plotted directly above the previous one at the same value of α. At this increment G_a and G_b have less than a 2 percent difference. Hence, delamination growth will occur in both directions simultaneously shown by the next G_a and G_b values being plotted at an increased value of α and β respectively. This procedure was continued until the delamination reached the leg.

A plot of normalized G^{SE} versus ϕ is shown in fig. 16 using the results of fig. 15. This plot details the variation in normalized G with delamination growth taking into account the two delamination fronts. The

delamination grows unstably until it has grown 60° around the curve. Total G then decreases and the growth becomes stable. Fig. 17 shows the variation of the G_I/G ratio as the delamination grows. Delamination growth is predominantly mode I, with pure mode I delamination growth at small delamination lengths.

Damage Progression in the Unidirectional Curved Laminates

Fig. 18 shows the normalized radial stresses plotted versus the normalized radius of the curved laminate with a delamination present at $(R-R_{inner})/t=0.42$. Three specific delamination lengths taken from fig. 16 are shown. As the delamination grows around the curved region the maximum radial stress in the newly forming inner and outer sub-laminates increases. At $\phi=90^o$ G is decreasing (fig. 16) and the maximum radial stress in the inner sub-laminate has reached a value similar to that responsible for the formation of the original delamination at R=6.25 mm as shown in fig. 9. Therefore, a new delamination should start in the inner sub-laminate as was observed experimentally, fig. 5. No further analysis of delamination growth from this location was conducted but it was assumed that this phenomenon would repeat sequentially and result in the final failure in fig. 5.

FAILURE LOAD PREDICTIONS AND DISCUSSION

To determine the maximum loads required to initiate damage in the unidirectional curved laminates, a suitable failure criterion must be used. Because of the high tensile strength in the fiber direction it is not necessary to consider the σ_θ stresses. Also, the values of $\tau_{r\theta}$ are an order of magnitude smaller than the σ_r stresses, and may be considered negligible. Therefore, it is sufficient for a strength approximation to assume that

delamination occurs when $\sigma_r = \sigma_{3f}$, where σ_{3f} is the interlaminar normal strength. However, as noted in the introduction, no suitable test for determining interlaminar normal strength has been developed. Hence, transverse isotropy must be considered and σ_{3f} approximated by σ_{2f}. From Fig. 9 the maximum normalized radial stress was given as $(\sigma_r\ w\ /P) = 4.37\ mm^{-1}$ occurring at an $(R-R_{inner})/t = 0.42$. Therefore, a range of failure loads per unit width can be determined:

$$\frac{P_f}{w} = \frac{\sigma_{2f}}{(\sigma_r\ w/P)} = 8.36 \leq \frac{P_f}{w} \leq 15.8\ N/mm \quad (mean = 12.3\ N/mm)$$

Table 1 shows that the agreement between the range of failure loads and the range of predicted loads was good. The mean failure load was over predicted by 15 percent. The predicted location of the delamination through the thickness was similar to that observed in the experimental work, Table 1.

The plot of normalized G versus ϕ shown in fig. 16 shows G beginning to decrease at $\phi \approx 60^0$. This type of decrease in G with delamination growth is often interpreted as an indication of stable delamination growth. However, the delamination usually grew well into the arm and leg, fig. 5. Delamination growth was shown in fig. 17 to be largely mode I dominated. Therefore, using the criteria that $G = G_c = G_{Ic}$ at failure a predicted load per unit width to further extend the delamination may be calculated. From fig. 16 at $\phi = 90^0$, $(G\ w^2/P^2) = 1.60$ E-2 mm/N:

$$\frac{P_f}{w} = \left[\frac{G_{Ic}}{\left(\frac{G\ w^2}{P^2}\right)}\right]^{1/2} = 2.01 \leq \frac{P_f}{w} \leq 2.41\ N/mm \quad (mean = 2.24\ N/mm)$$

where G_{Ic} was obtained from the DCB specimens. These values of applied load per unit width are well below the load already applied to the curved laminate,

indicating that the delamination will extend into the arm and the leg until G decreases below G_c.

At a delamination length of ϕ=90^0 the maximum normalized radial stress in the inner sublaminate from fig. 18 was $(\sigma_r$ w/P)= 4.10 N/mm^{-1} at an $(R-R_{inner})/t \approx 0.20$. A new delamination will occur at a load per unit width between 8.90 and 16.8 N/mm. This range of loads is approximately equal to the range of loads already on the specimen. Also, the predicted location of the second delamination is similar to that shown in fig. 5b. Hence, damage accumulating at different locations through the thickness would be expected to be unstable, as observed experimentally.

SUMMARY

This paper investigated delamination failure in curved composite laminates. A unidirectional curved laminate was tested quasi-statically and analyzed. These laminates failed unstably by delaminations radiating around the curved region of the laminate and accumulating at different locations through the thickness until most of the bending stiffness was lost. Delamination was assumed to initiate at the location of the highest radial stress within the curved region. A closed form curved beam elasticity solution and a finite element analysis (FEA) were used to determine the location of the highest radial stress. A strength-based failure criteria predicted the failure load for the onset of the first delamination. The FEA was then used to determine the change in strain energy release rate, G, with delamination growth in both directions from the initiation site. The strain energy release rate was found to be predominantly mode I. Strain energy release rate initially increased with delamination growth and then decreased

as the delamination reached the straight arm and leg. However, the value of G with delamination fully extended around the curved region was larger than the critical value of G determined from Double Cantilever Beam specimens. Thus, delamination growth was predicted to extend into the arm and leg of the laminate as observed experimentally. As the initial delamination grew around the curved region, the maximum radial stress in the newly forming inner sublaminate increased to a sufficient level to cause a new delamination to initiate in the sublaminate with no increase in applied load. This failure sequence was also observed experimentally.

REFERENCES

1. O'Brien, T.K., "Mixed Mode Strain Energy Release Rate Effects on Edge Delamination of Composites," **Effects of Defects in Composite Materials**, ASTM STP 836,D.J. Wilkins, ed., American Society for Testing and Materials, Philadelphia, PA, 1984, pp. 125-142.
2. Wang, A.S.D., "Strength, Failure and Fatigue Analysis of Laminates," **Composites**, Engineering Materials Handbook, Vol.1, 1987, pp. 236-251.
3. **Delamination and Debonding of Materials**, ASTM STP 876, W.S. Johnson, ed., American Society for Testing and Materials, Philadelphia, PA, 1985.
4. Lowry, D.W., Krebs, N.E., and Dobyns, A.L., "Design, Fabrication and Test of Composite Curved Frames for Helicoptor Fuselage Structure," NASA CR 172438, October 1984.
5. Chang, F.K., and Springer, G.S., "The Strengths of Fiber Reinforced Composite Bends," **Journal of Composite Materials**, Vol. 20, January 1986, pp. 30-45.

6. Mabson, G.E., and Neall, E.P., III, "Analysis and Testing of Composite Aircraft Frames for Interlaminar Tension Failure," Presented at the National Specialist's Meeting on Rotary Wing Test Technology of the American Helicoptor Society, Bridgeport, Connecticut, March 15-16, 1988.

7. Ko, W.L., "Delamination Analysis of Semicircular Laminated Composite Curved Bars Subjected to Bending," NASA TM 4026, April 1988.

8. Sun, C.T., and Kelly, S.R., "Failure in Composite Angle Structures Part I: Initial Failure," **Journal of Reinforced Plastics and Composites**, Vol. 7, May 1988, pp. 220-232.

9. Kedward, K.T., Wilson, R.S. and McLean, S.K., " The Flexure of Simply Curved Composite Shapes," To appear in **Composite Materials: Testing and Design, 9th Volume**, ASTM STP 1059, S.P. Garbo, ed., American Society for Materials and Testing, Philadelphia, PA.

10. Sun, C.T., and Kelly, S.R., "Failure in Composite Angle Structures Part II: Onset of Delamination," **Journal of Reinforced Plastics and Composites**, Vol. 7, May 1988, pp. 233-244.

11. DiNicola, A.J., Halvorson, R. M., Kassapoglou, C., and Levine, L.T., "Developments in Design and Analysis of Composite Structures with Delaminations at Sikorsky Aircraft," Internal Report, Structures Research Section, January 1989, Sikorsky Aircraft, CT.

12. O'Brien, T.K. "Towards a Damage Tolerance Philosophy for Composite Materials and Structures," To appear in **Composite Materials: Testing and Design, 9th Volume**, ASTM STP 1059, S.P. Garbo, ed., American Society for Testing and Materials, Philadelphia, PA. (Also available as NASA TM 100548, April 1988).

13. O'Brien, T.K., Rigamonti, M., and Zanotti, C., "Tension Fatigue Analysis and Life Prediction for Composite Laminates," **International Journal of Fatigue**, Vol. 11, No. 6, November 1989, pp. 379-394.

14. Murri, G.B., Salpekar, S.A., and O'Brien, T.K., "Fatigue Delamination Onset Prediction in Tapered Composite Laminates," Presented at the 3rd ASTM Symposium on Composite Materials: Fatigue and Fracture, Lake Buena Vista, FL, November 5-10, 1989. (Also available as NASA TM 101673, December 1989).

15. Murri, G.B., O'Brien, T.K., and Salpekar, S.A., "Tension Fatigue of Glass/Epoxy and Graphite/Epoxy Tapered Laminates," Presented at the 46th Annual American Helicopter Society Forum, Washington, D.C., May 21-23, 1990.

16. Martin, R.H., and Murri, G.B., "Characterization of Mode I and Mode II Delamination Growth and Thresholds in Graphite/PEEK," To appear in **Composite Materials: Testing and Design, 9th Volume**, ASTM STP 1059, S.P. Garbo, ed., American Society for Testing and Materials, Philadelphia, PA. (Also available as NASA TM 100577, April 1988).

17. Martin, R.H., "Effect of Initial Delamination on G_{Ic} and G_{Ith} Values Obtained from Glass/Epoxy Double Cantilever Beam Tests," Proceedings of the American Society for Composites Third Technical Conference, Seattle, WA, September 26-29, 1988, Technomic, Lancaster, PA, pp. 688-700.

18. Martin, R.H., and O'Brien, T.K., "Characterizing Mode I Fatigue Delamination of Composite Materials," Proceedings of the American Society for Composites Fourth Technical Conference, Blacksburg, VA, October 3-6, 1989, Technomic, Lancaster, PA, pp. 257-266.

19. Martin R.H., "Characterizing Fatigue Delamination of Composite Materials Using the Double Cantilever Beam Specimen," NASA CR 181991, 1990.

20. Cantwell, W.J., Davies, P., and Kausch, H.H., "Cooling Rate Effects in Carbon Fibre/PEEK Composites," Presented at the 3rd ASTM Symposium on Composite Materials: Fatigue and Fracture, Lake Buena Vista, FL, November 5-10, 1989.

21. DOD/NASA Advanced Composites Design Guide, Vol. IVa - Materials, 1st Edition, Contract No. F33615-78C-3203, Flight Dynamics Lab., Wright Patterson Air Force Base, July 1983.

22. Lekhnitskii, S.G., "**Anisotropic Plates**," Gordon and Breach Science Publishers, New York, 1968.

23. NASTRAN Users Manual, Version 65, Document No. MSR-39, MacNeal-Schwendler Corporation, November 1985.

24. Rybicki, E.F., and Kanninen, M.F., "A Finite Element Calculation of Stress Intensity Factors by a Modified Crack Closure Integral," **Engineering Fracture Mechanics**, Vol. 9, 1977, pp. 931-938.

Appendix A - Closed Form Elasticity Solution for the Stresses in an Anisotropic Curved Beam

Reference 22 gave the elasticity solutions for the radial, tangential, and shear stresses in a curved beam subjected to pure bending and an end force. The beam was assumed to possess cylindrical anisotropy and its pole is located at the center of the arcs which form the beam contour. The expressions are repeated here with the notation given in the Nomenclature and in fig. 6

Stresses Caused by End Moment M

$$\sigma_r^M = \frac{-M}{d^2 w g}\left[1 - \frac{1-\left(\frac{c}{d}\right)^{\kappa+1}}{1-\left(\frac{c}{d}\right)^{2\kappa}}\left(\frac{r}{d}\right)^{\kappa-1} - \frac{1-\left(\frac{c}{d}\right)^{\kappa-1}}{1-\left(\frac{c}{d}\right)^{2\kappa}}\left(\frac{c}{d}\right)^{\kappa+1}\left(\frac{d}{r}\right)^{\kappa+1}\right] \quad \text{(A1)}$$

$$\sigma_\theta^M = \frac{-M}{d^2 w g}\left[1 - \frac{1-\left(\frac{c}{d}\right)^{\kappa+1}}{1-\left(\frac{c}{d}\right)^{2\kappa}}\kappa\left(\frac{r}{d}\right)^{\kappa-1} + \frac{1-\left(\frac{c}{d}\right)^{\kappa-1}}{1-\left(\frac{c}{d}\right)^{2\kappa}}\kappa\left(\frac{c}{d}\right)^{\kappa+1}\left(\frac{d}{r}\right)^{\kappa+1}\right] \quad \text{(A2)}$$

$$\tau_{r\theta}^M = 0 \quad \text{(A3)}$$

where

$$g = \frac{1-\left(\frac{c}{d}\right)^2}{2} - \frac{\kappa}{\kappa+1}\frac{\left[1-\left(\frac{c}{d}\right)^{\kappa+1}\right]^2}{\left[1-\left(\frac{c}{d}\right)^{2\kappa}\right]} + \frac{\kappa\left(\frac{c}{d}\right)^2}{\kappa-1}\frac{\left[1-\left(\frac{c}{d}\right)^{\kappa-1}\right]^2}{\left[1-\left(\frac{c}{d}\right)^{2\kappa}\right]} \quad \text{(A4)}$$

and the anisotropic parameter is defined as

$$\kappa = \left[\frac{E_\theta}{E_r}\right]^{1/2} \quad \text{(A5)}$$

Stresses Caused by End Force P

$$\sigma_r^P = \frac{P}{r\ w\ g_1}\left[\left(\frac{r}{d}\right)^{\omega} + \left(\frac{c}{r}\right)^{\omega} - 1 - \left(\frac{c}{d}\right)^{\omega}\right]\cos\theta \tag{A6}$$

$$\sigma_\theta^P = \frac{P}{r\ w\ g_1}\left[(1+\omega)\left(\frac{r}{d}\right)^{\omega} + (1-\omega)\left(\frac{c}{r}\right)^{\omega} - 1 - \left(\frac{c}{d}\right)^{\omega}\right]\cos\theta \tag{A7}$$

$$\tau_{r\theta}^P = \frac{-P}{r\ w\ g_1}\left[\left(\frac{r}{d}\right)^{\omega} + \left(\frac{c}{r}\right)^{\omega} - 1 - \left(\frac{c}{d}\right)^{\omega}\right]\sin\theta \tag{A8}$$

where

$$g_1 = \frac{2}{\omega}\left[1 - \left(\frac{c}{d}\right)^{\omega}\right] + \left[1 + \left(\frac{c}{d}\right)^{\omega}\right]\ln\left(\frac{c}{d}\right) \tag{A9}$$

and the anisotropic parameter, ω, is defined as

$$\omega = \left[1 + \frac{E_\theta}{E_r}(1-2\nu_{r\theta}) + \frac{E_\theta}{G_{r\theta}}\right]^{1/2} \tag{A10}$$

Panel No. - Specimen No.	Maximum load per unit width (N/mm)	$\frac{(R - R_{inner})}{t}$ of first delamination
6-4	7.62	0.49
6-8	14.60	0.48
7-1	8.68	0.46
7-2	10.05	0.48
7-6	13.36	0.48
7-7	13.09	0.35
7-8	7.23	0.33

$$7.23 \leq \frac{P_f}{w} \leq 14.60 \text{ N/mm}$$

Mean = 10.66 N/mm

Table 1 Experimental Failure Loads in the Curved Laminates

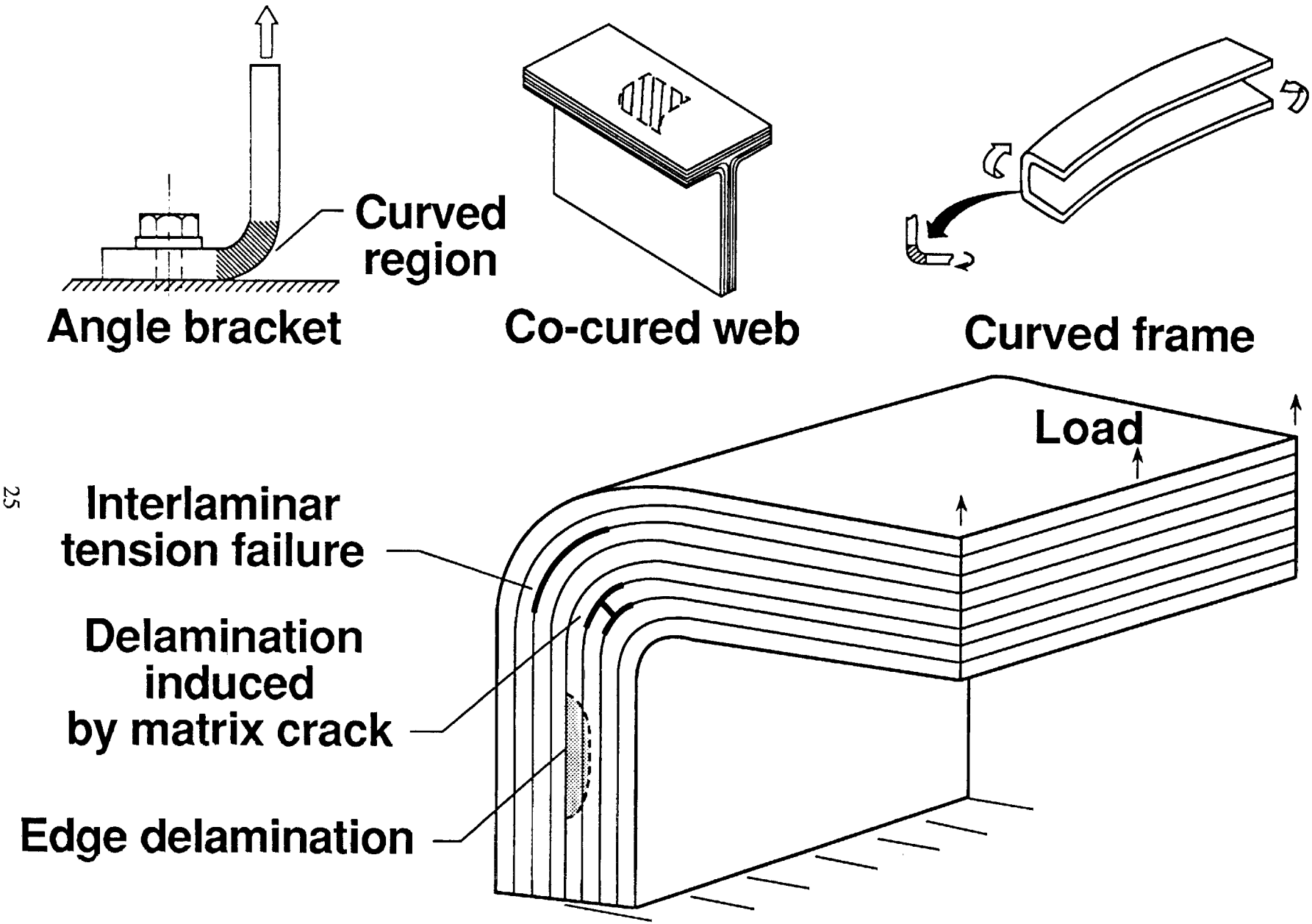

Fig. 1. - Curved laminate configurations and failures.

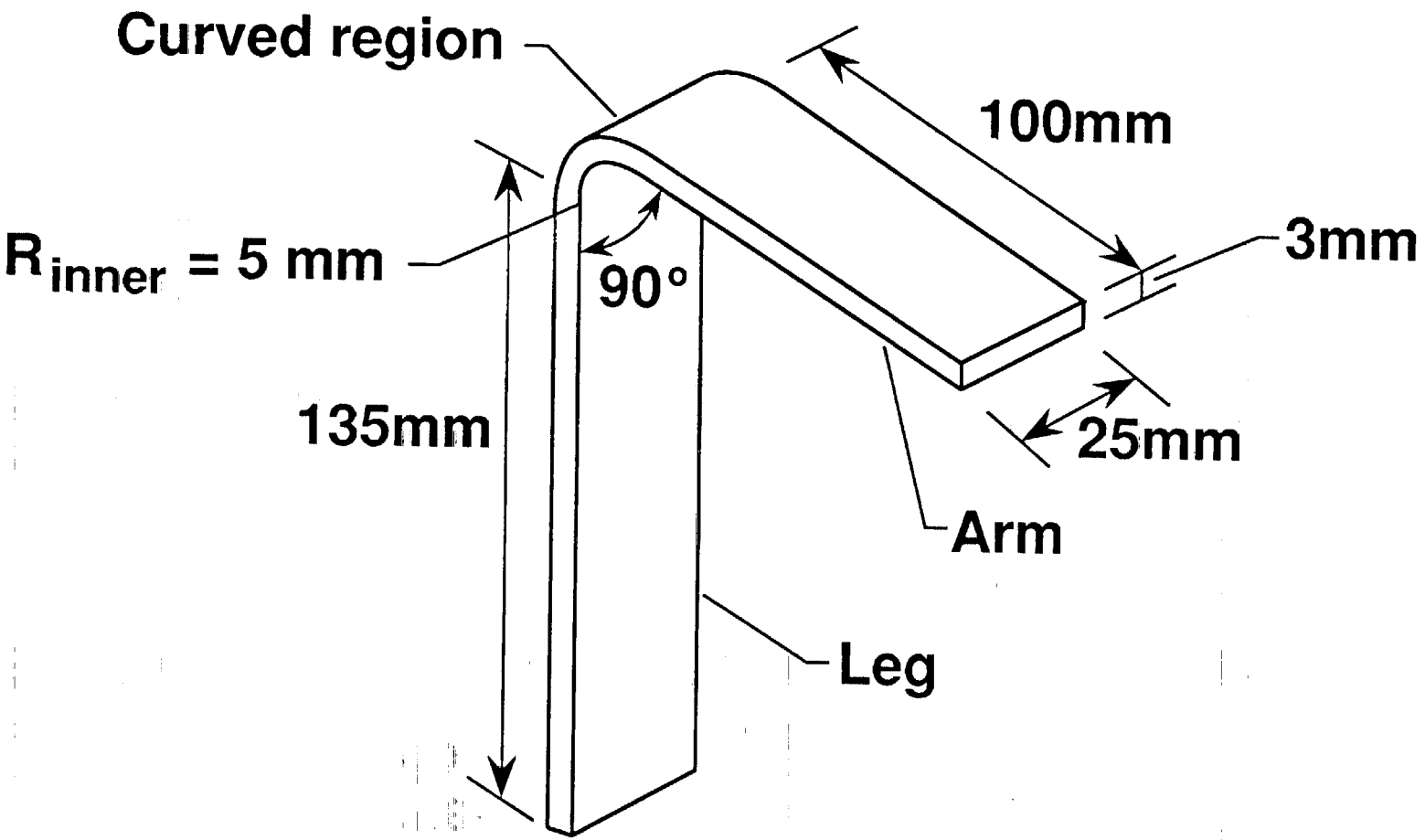

Fig. 2. - Dimensions of curved laminate.

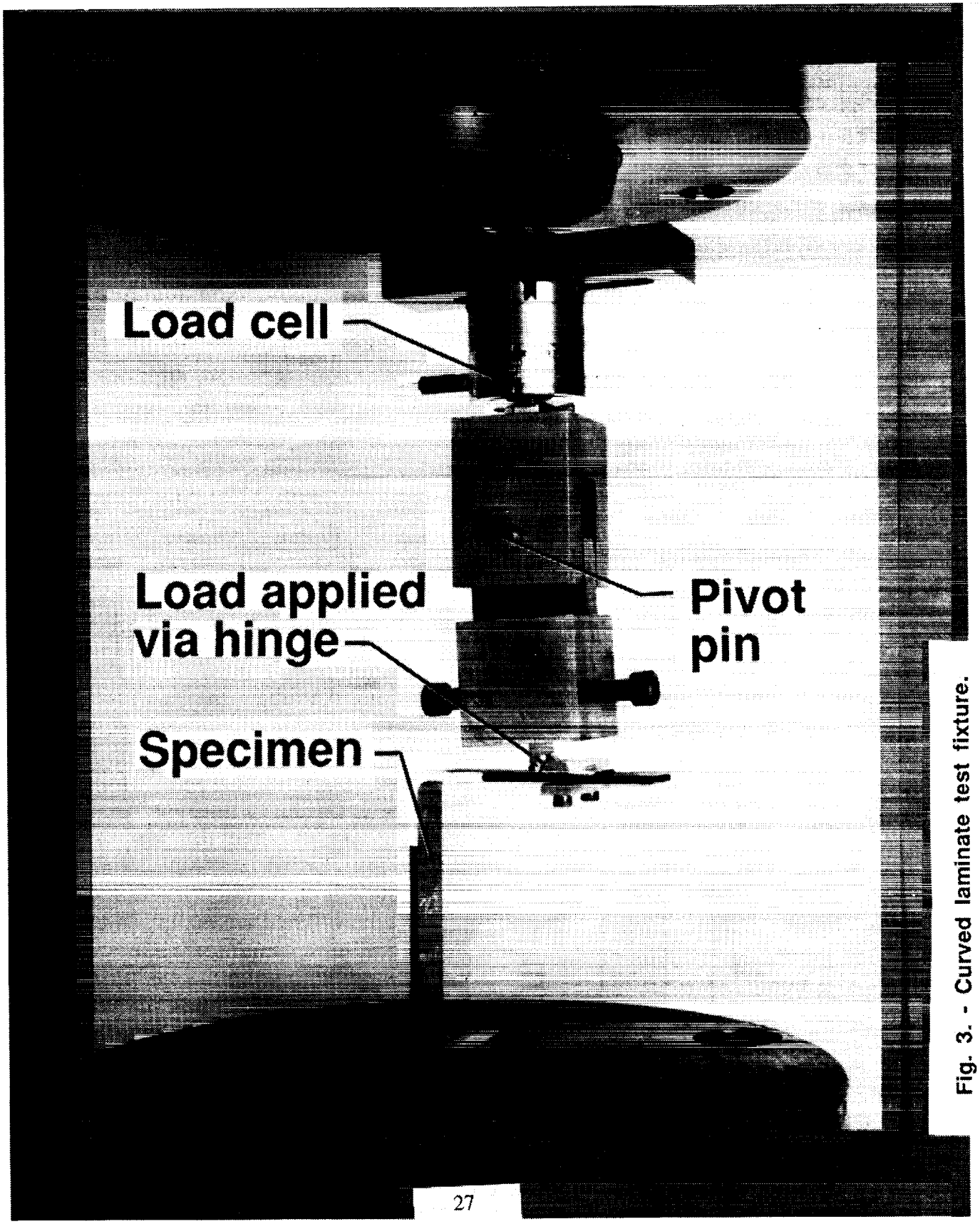

Fig. 3. - Curved laminate test fixture.

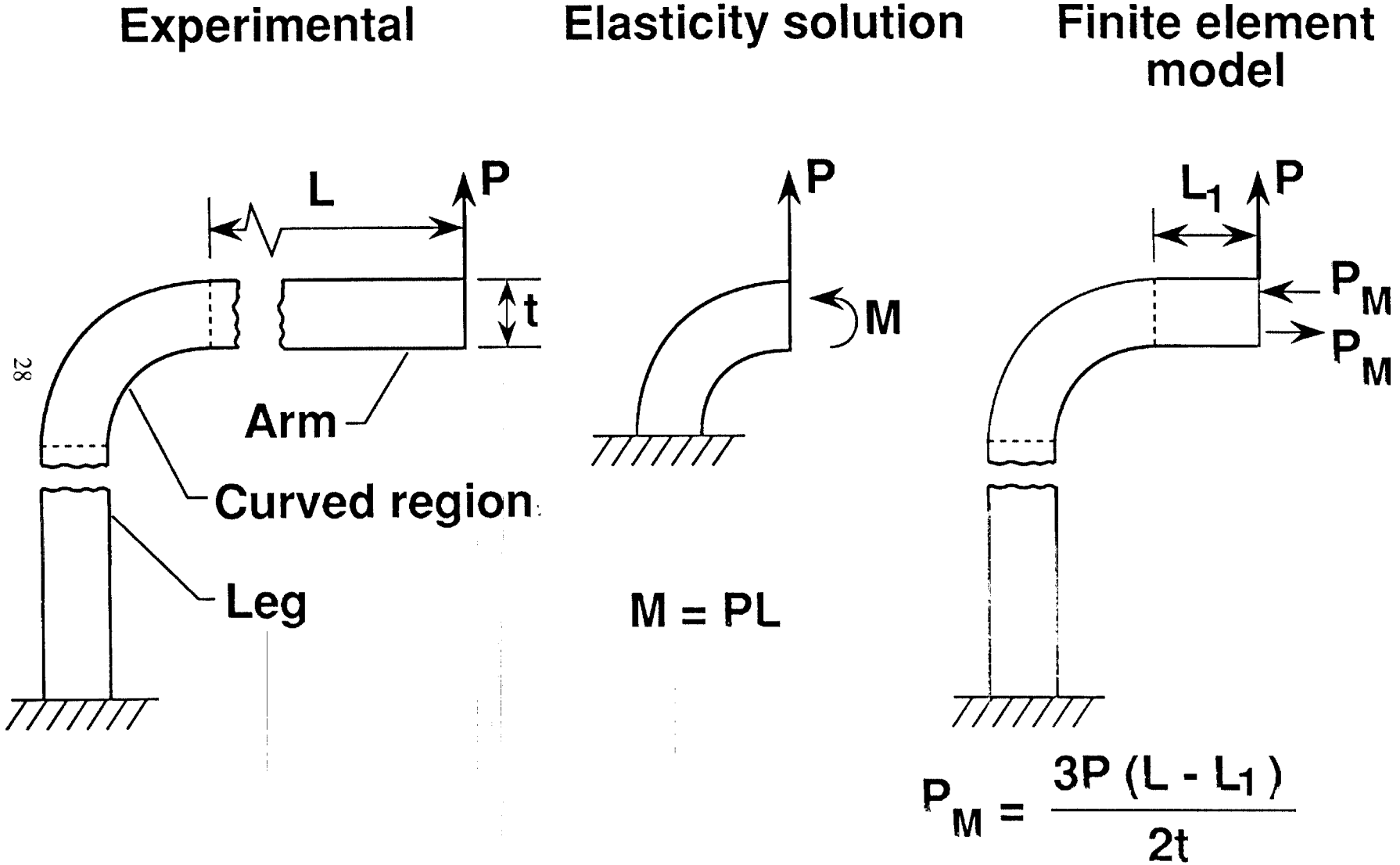

Fig. 4. - Curved laminate models.

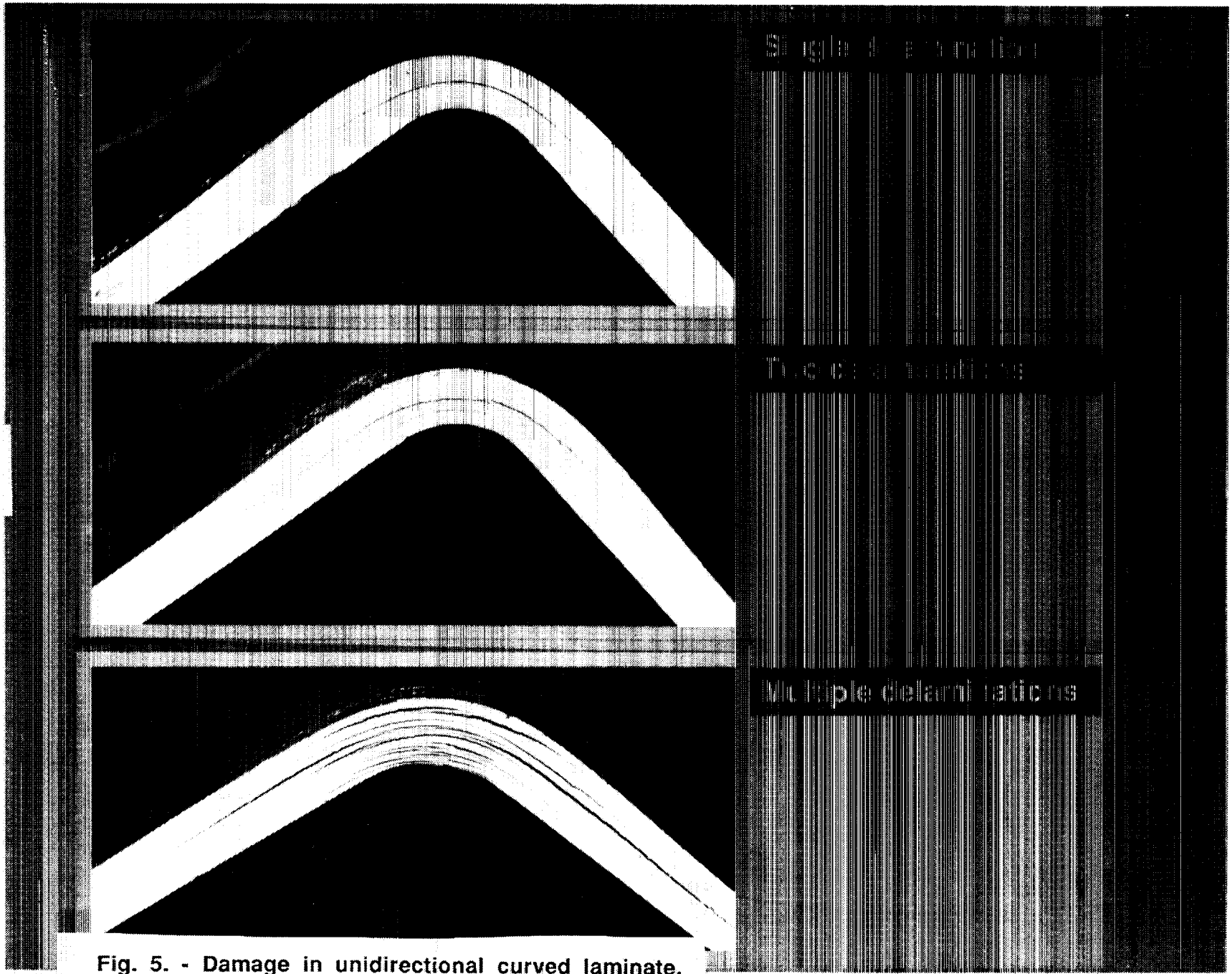

Fig. 5. - Damage in unidirectional curved laminate.

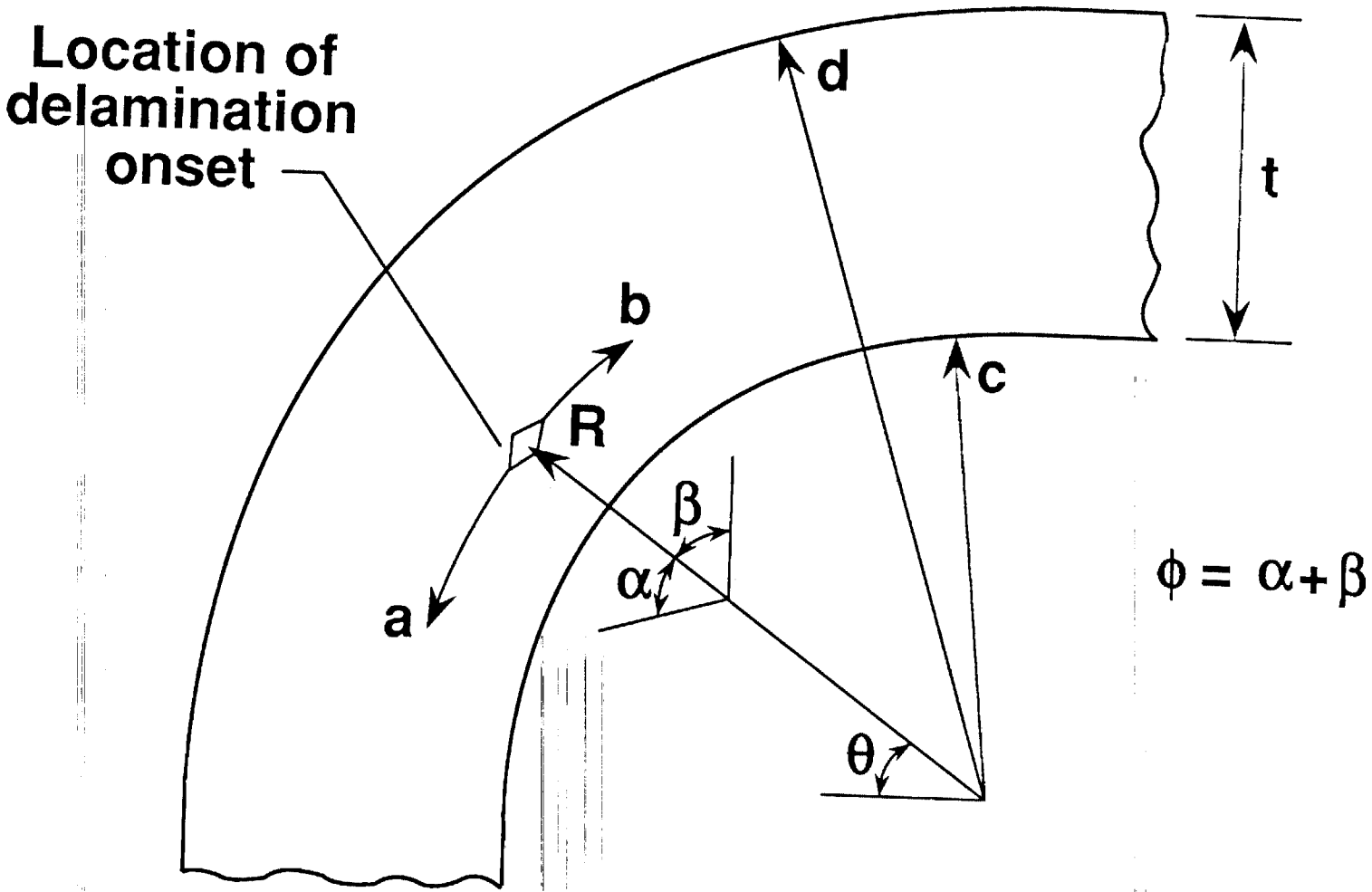

Fig. 6. - Notation for unidirectional curved laminate.

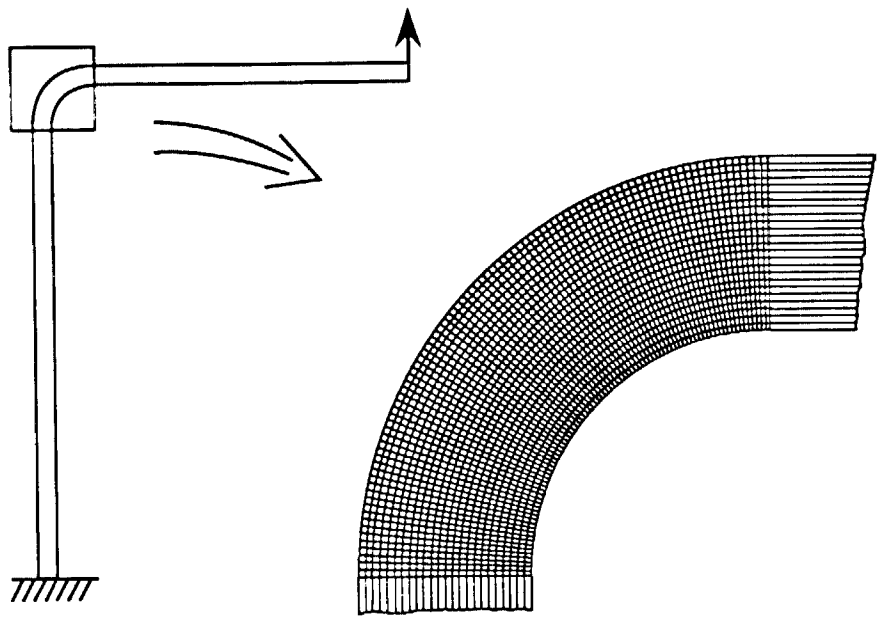

7 a Model 1

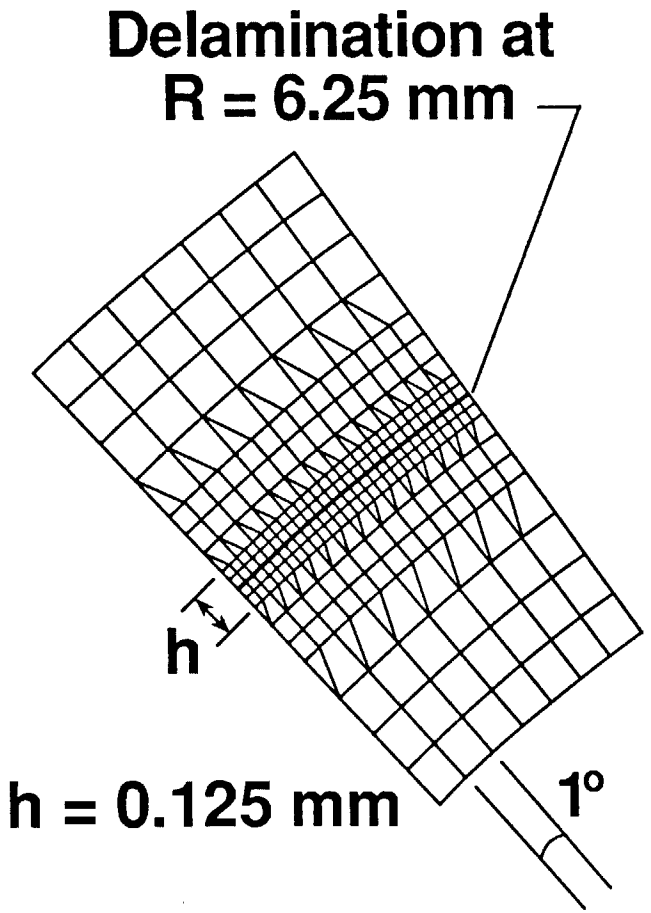

7 b Model 2

Fig. 7. - Finite-element mesh.

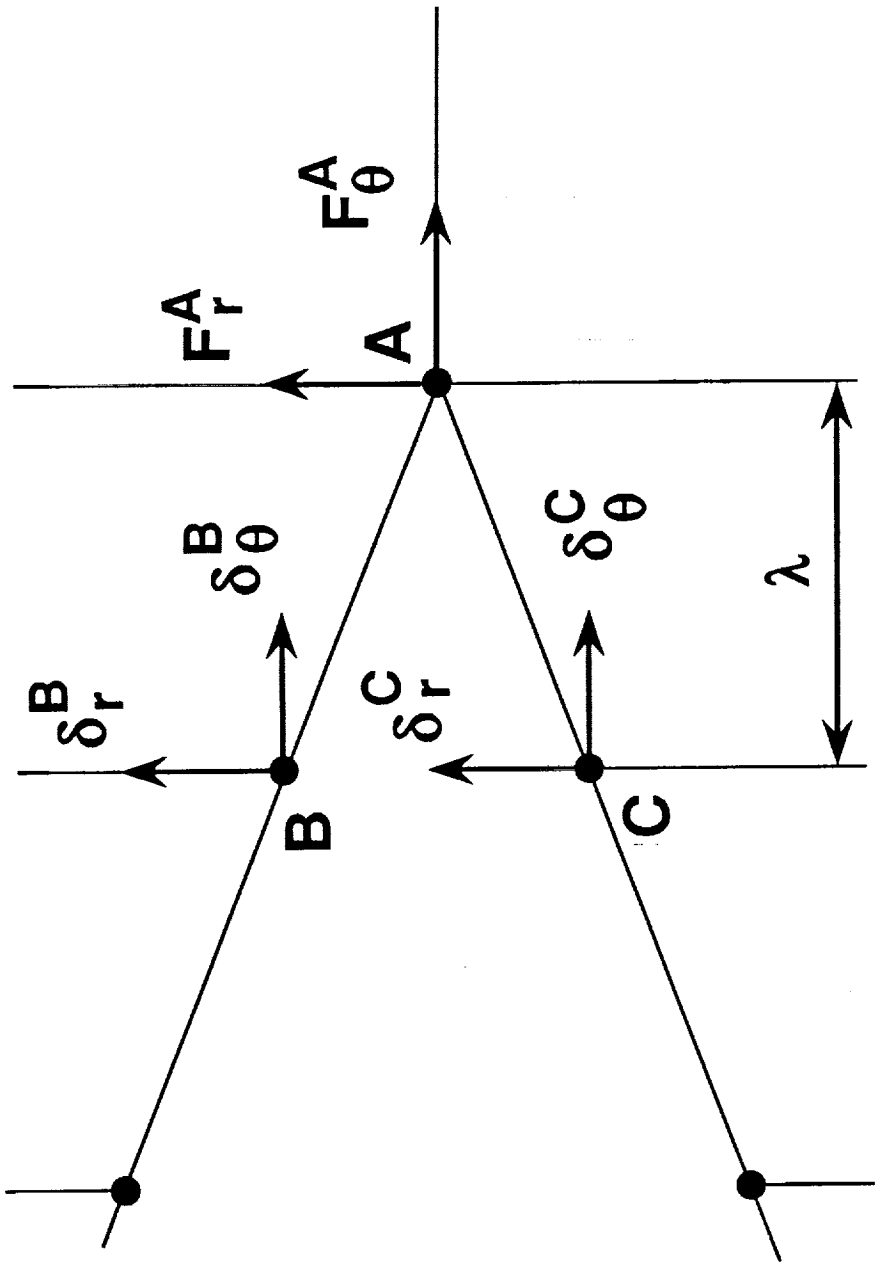

Fig. 8. - Virtual crack closure notation.

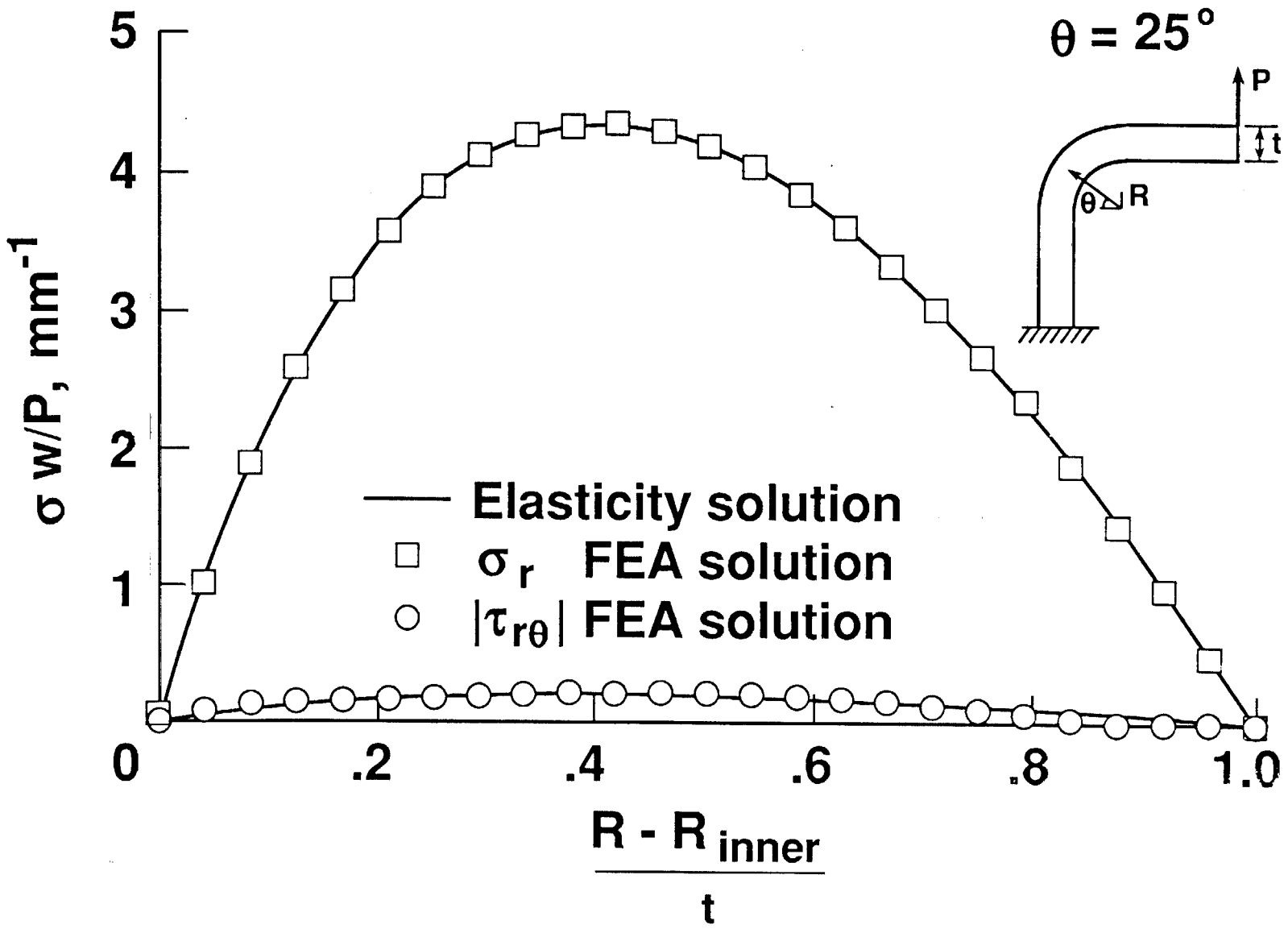

Fig. 9. - Interlaminar stresses through thickness.

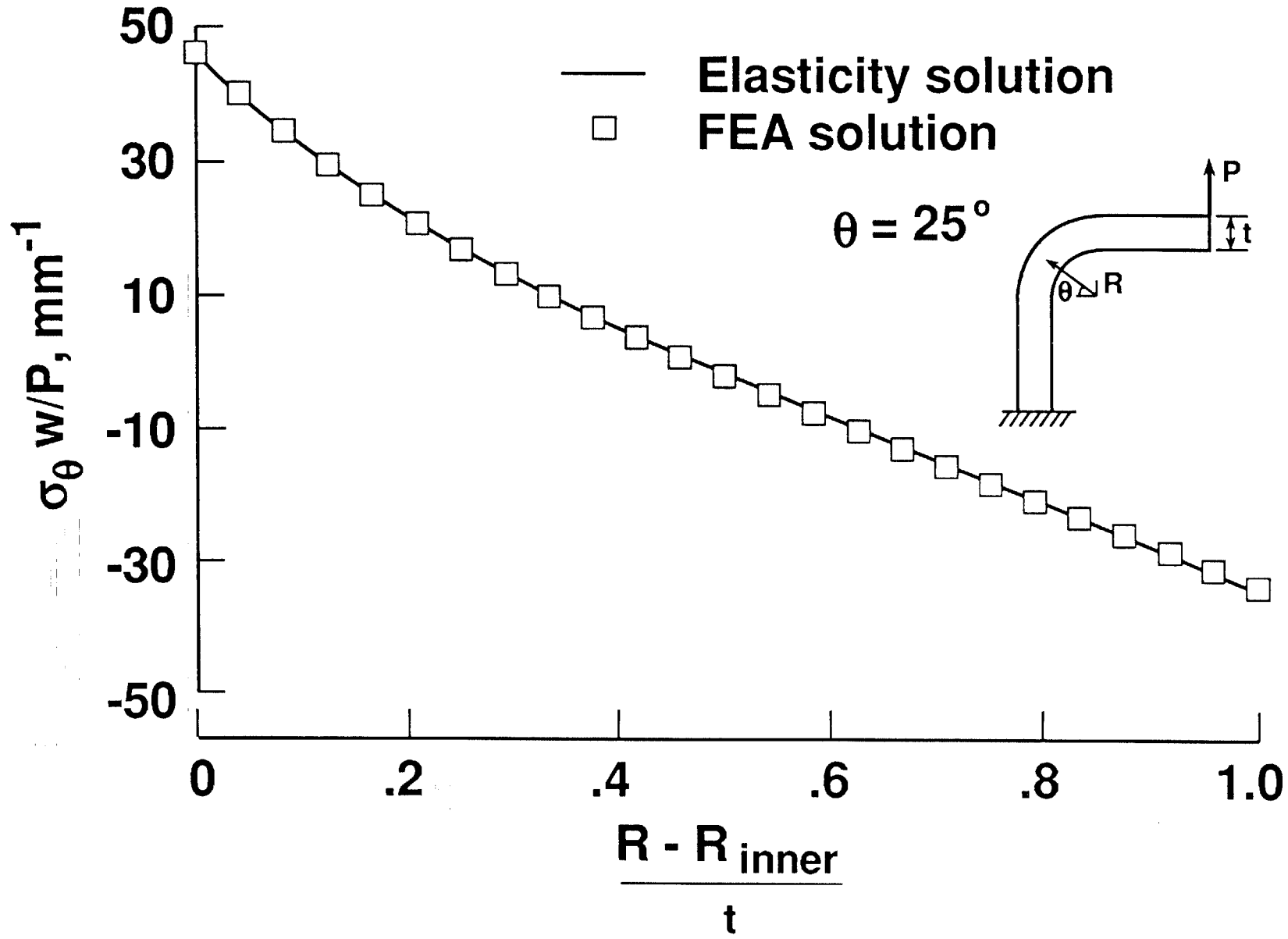

Fig. 10. - Tangential stress through thickness.

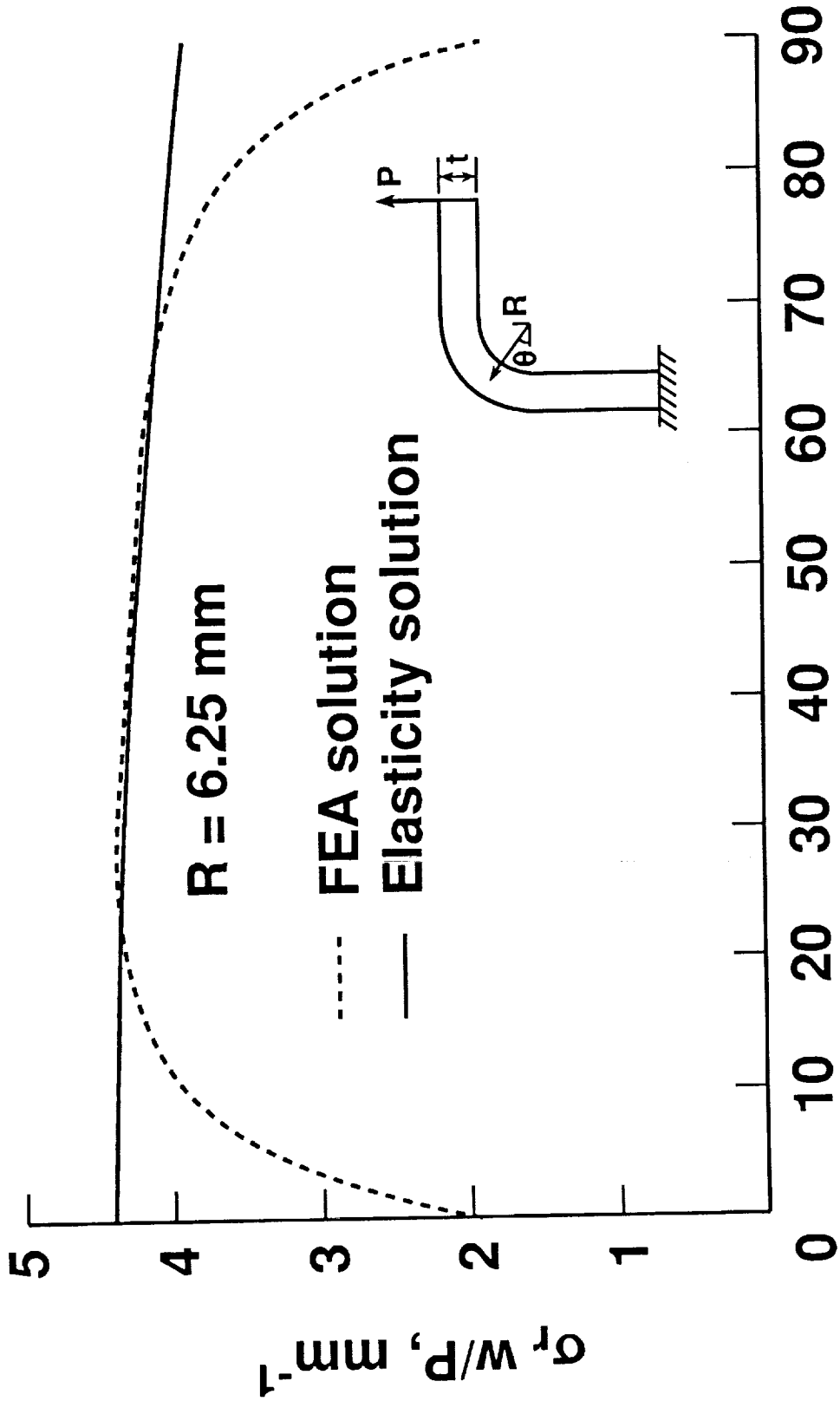

Fig. 11. - Radial stress around curved region.

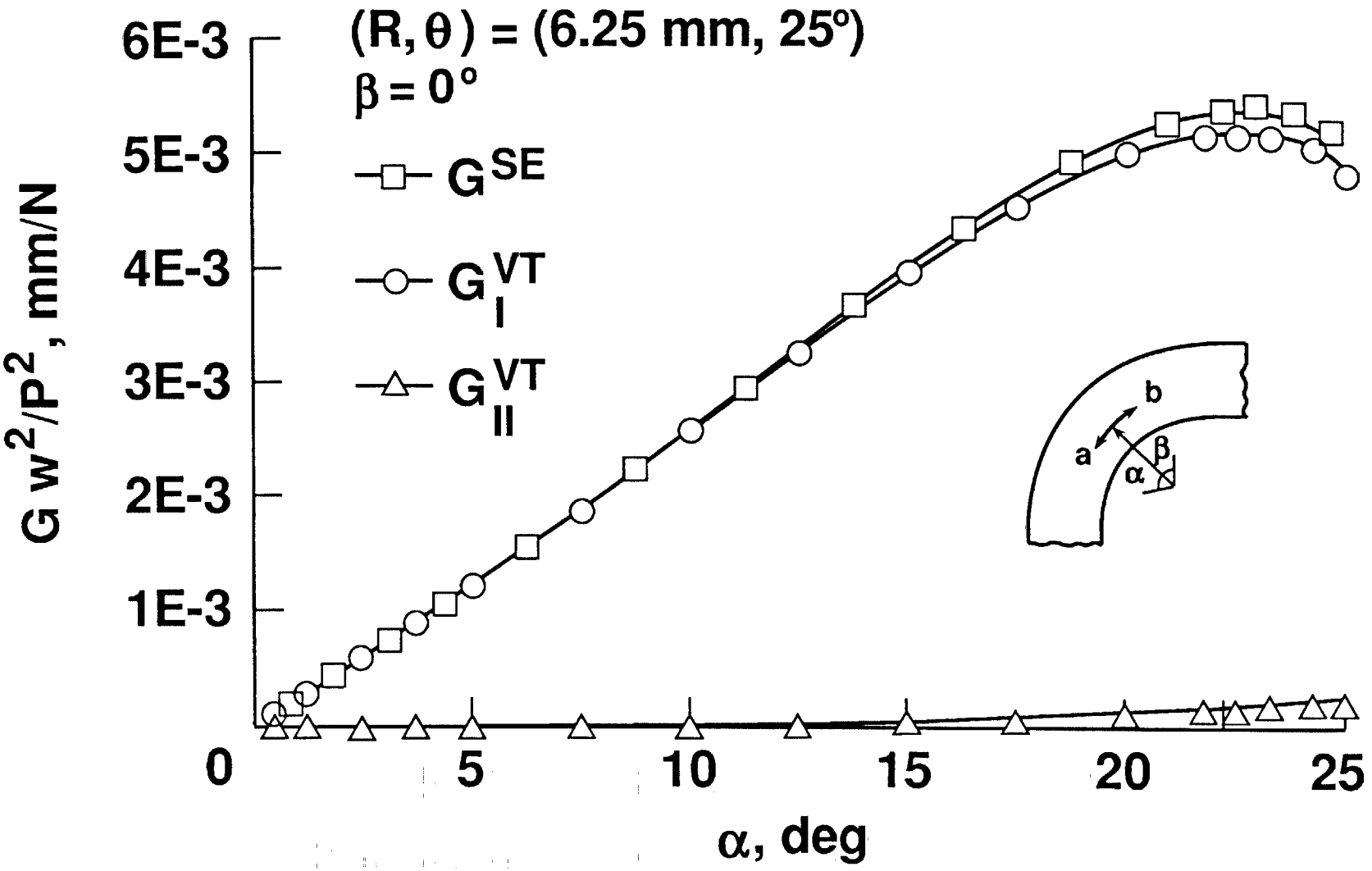

Fig. 12. - G Variation with delamination growth in the α direction.

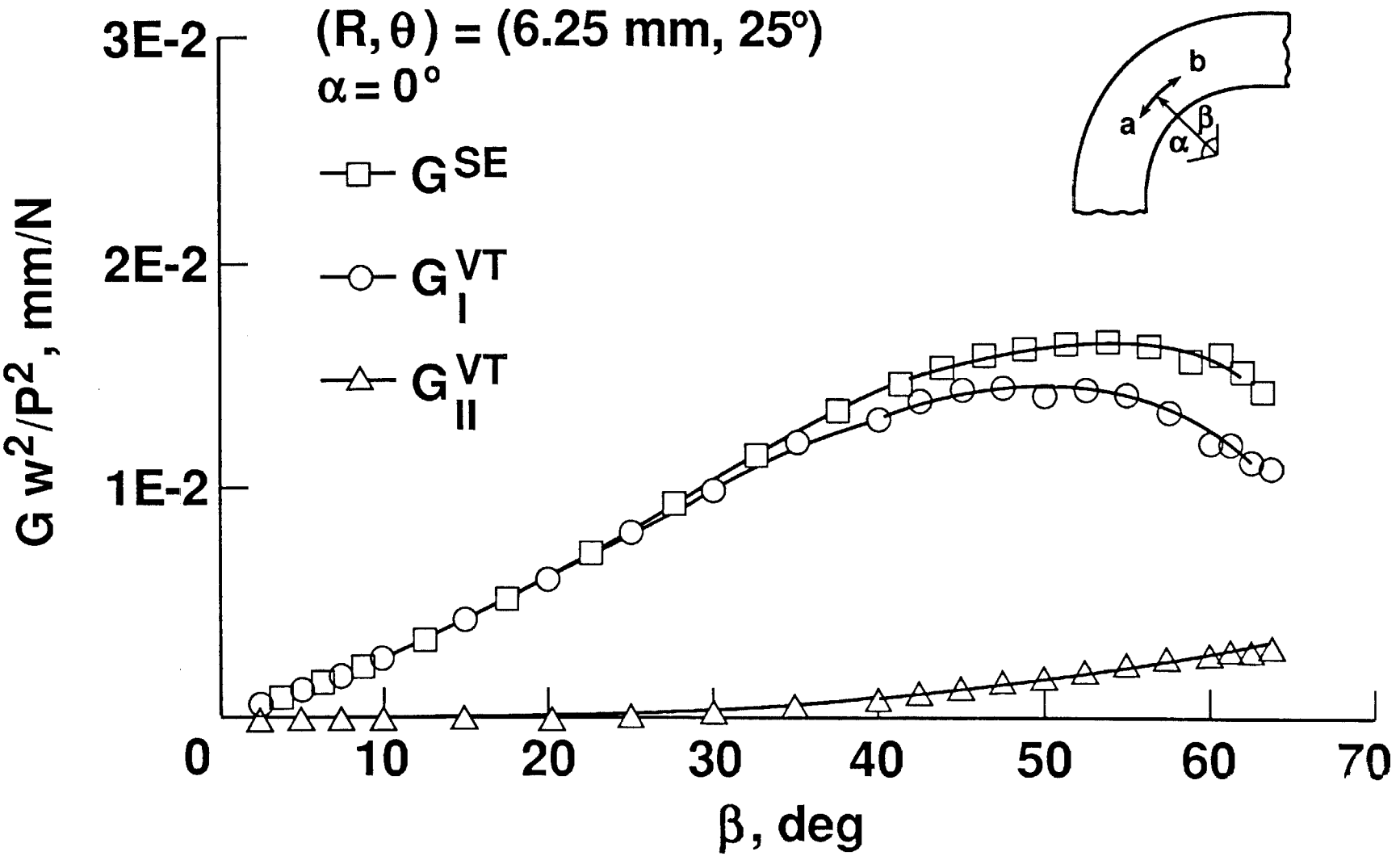

Fig. 13. - G Variation with delamination growth in the β direction.

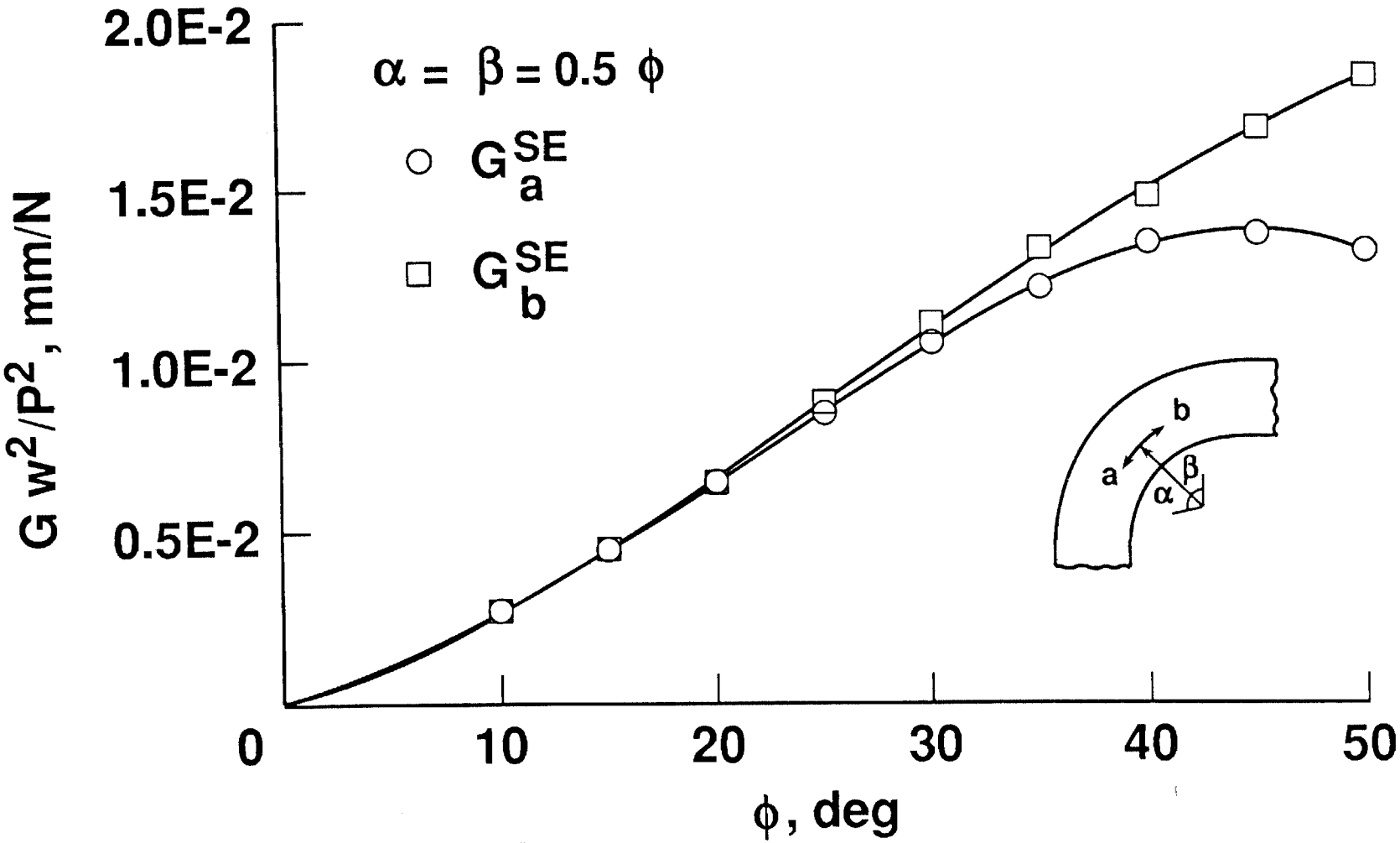

Fig. 14. - G Variation with delamination growth in the α and β direction.

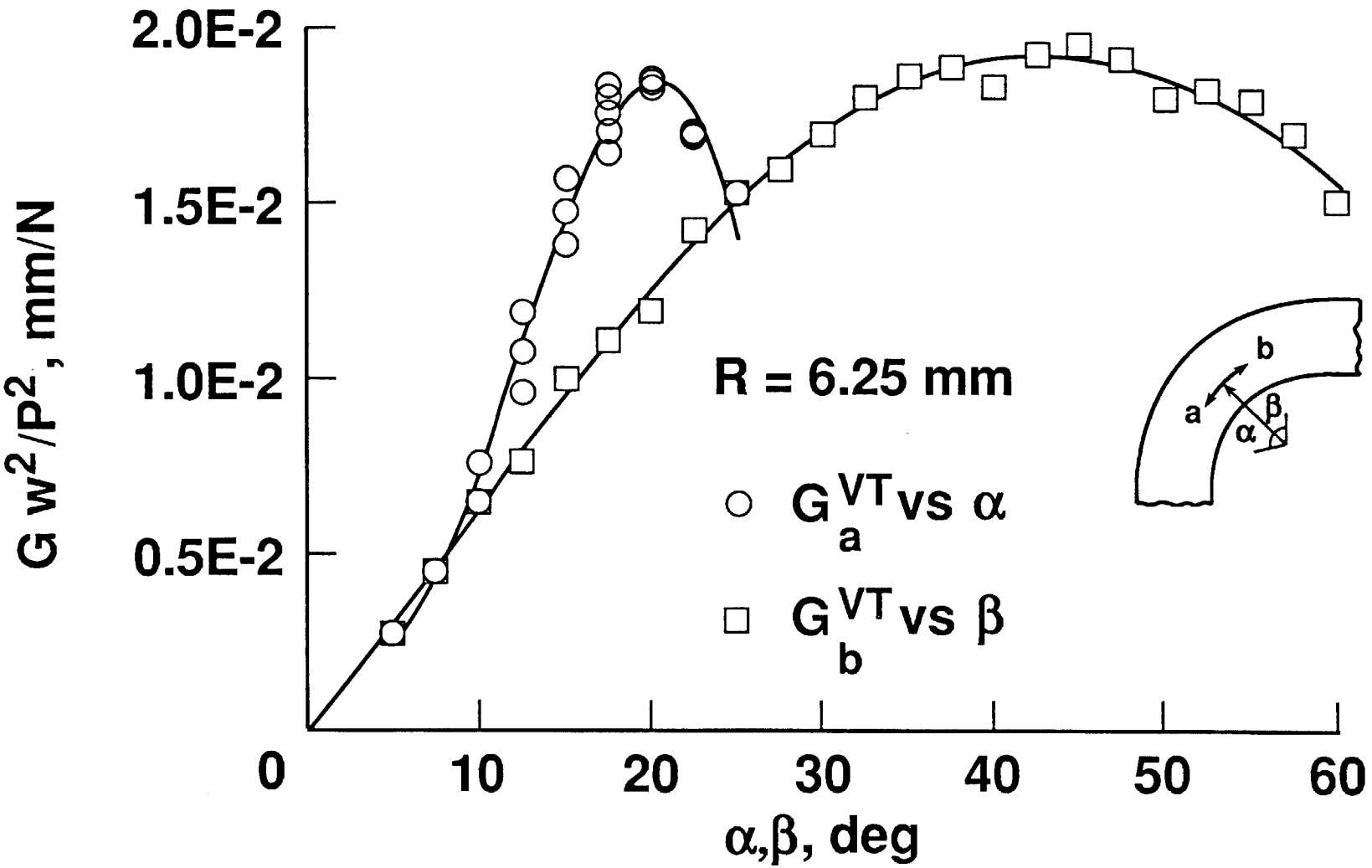

Fig. 15. - G_a versus α G_b versus β.

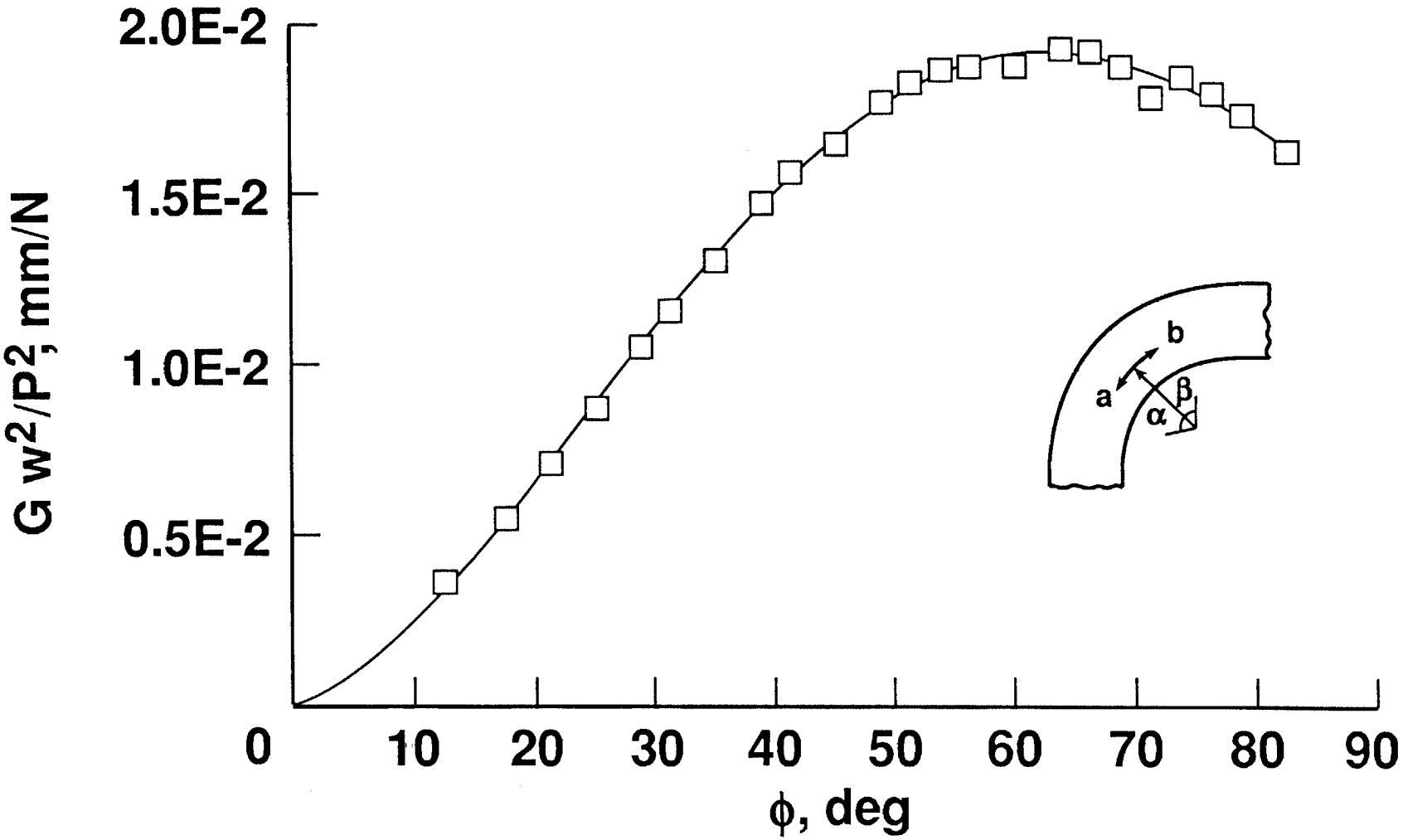

Fig. 16. - G Variation with delamination growth in both directions.

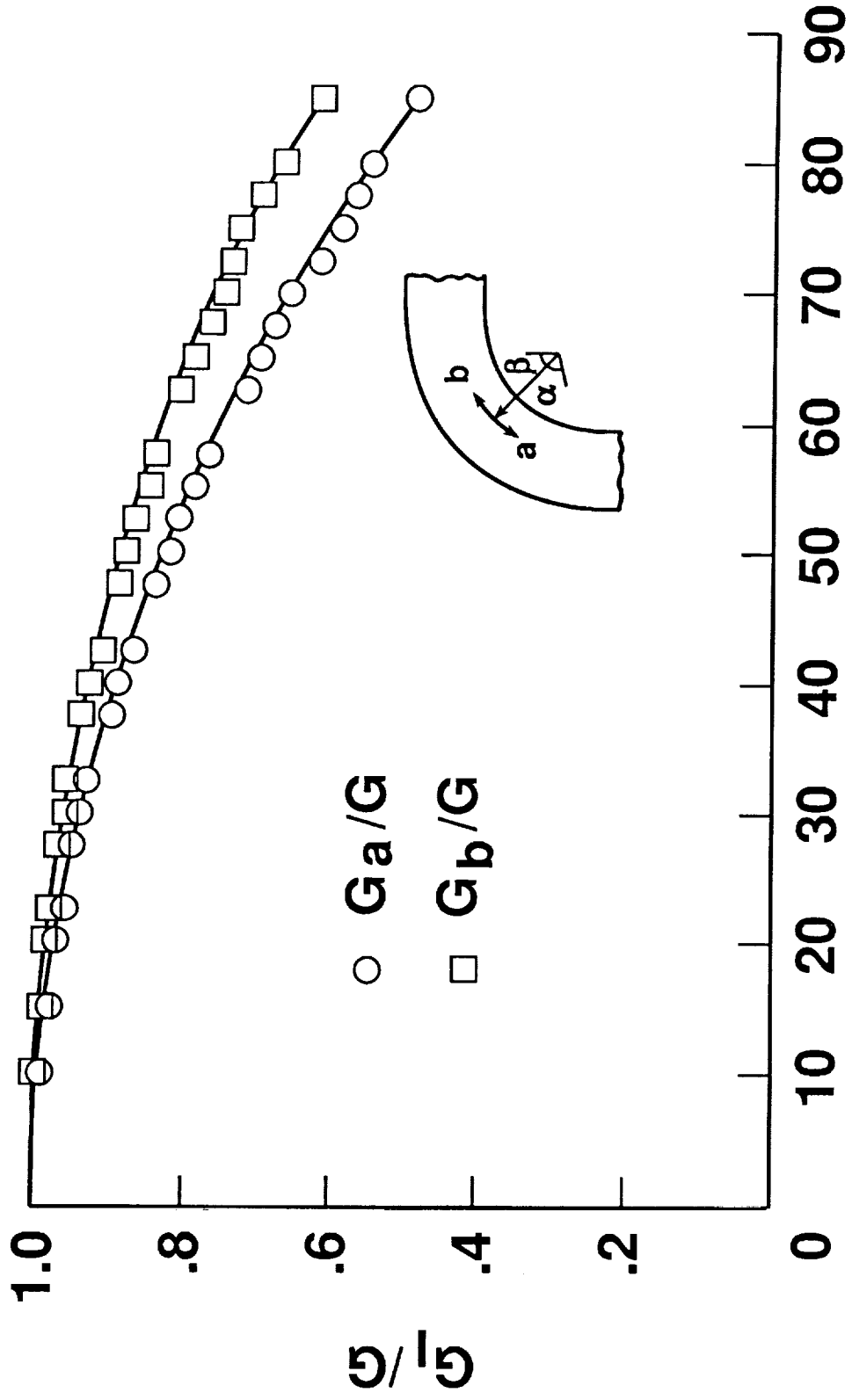

Fig. 17. - G_I/G Ratio with delamination growth.

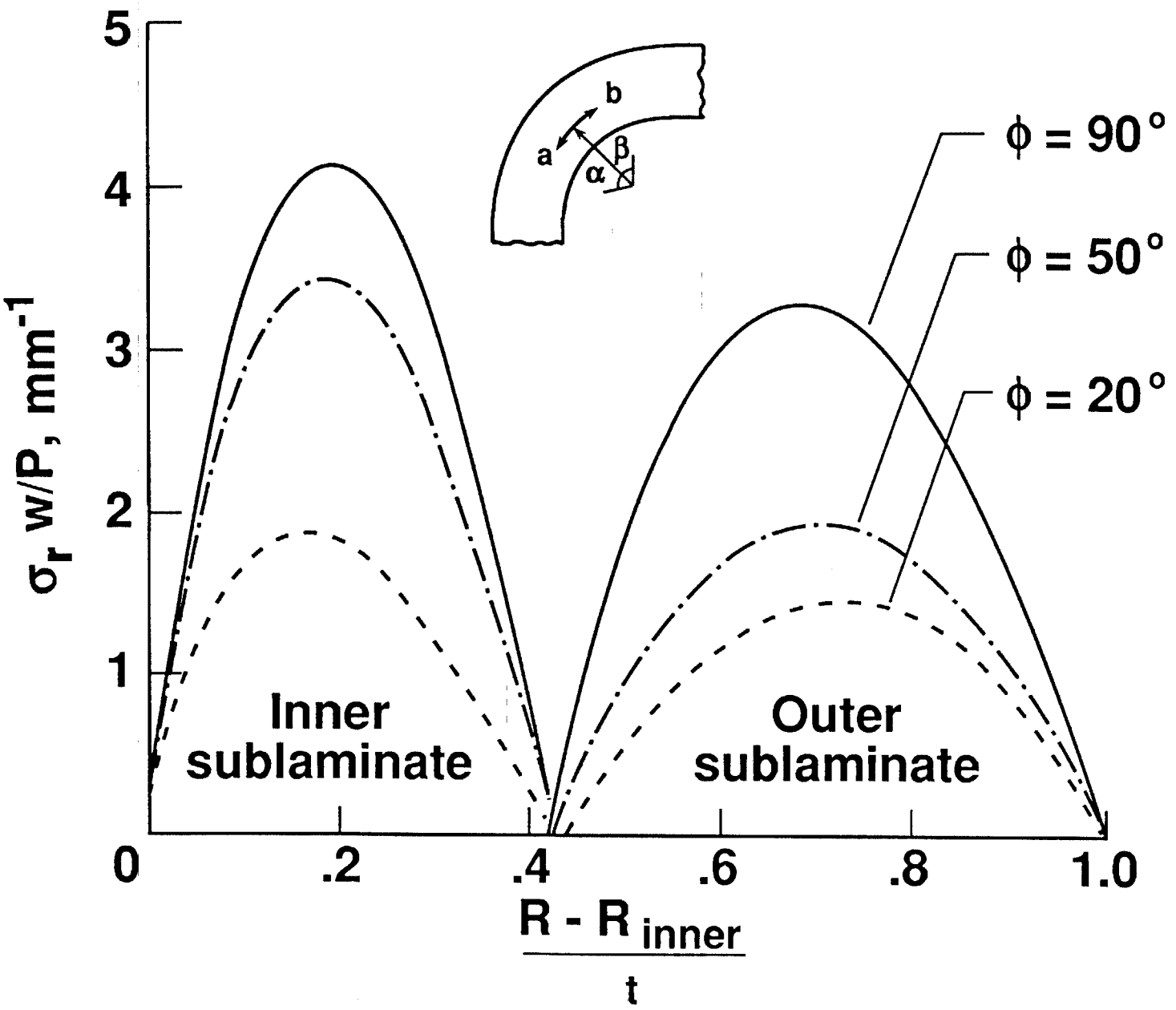

Fig. 18. - Radial stress through thickness in presence of a delamination.

NASA National Aeronautics and Space Administration

Report Documentation Page

1. Report No.	2. Government Accession No.	3. Recipient's Catalog No.
NASA CR-182018		

4. Title and Subtitle	5. Report Date
Delamination Failure in a Unidirectional Curved Composite Laminate	April 1990
	6. Performing Organization Code

7. Author(s)	8. Performing Organization Report No.
Roderick H. Martin	
	10. Work Unit No.
	505-63-01-05

9. Performing Organization Name and Address	11. Contract or Grant No.
Analytical Services and Materials, Inc. Hampton, VA 23666	NAS1-18599
	13. Type of Report and Period Covered
12. Sponsoring Agency Name and Address National Aeronautics and Space Administration Langley Research Center Hampton, VA 23665-5225	Contractor Report
	14. Sponsoring Agency Code

15. Supplementary Notes

Langley Technical Monitor: Charles E. Harris

16. Abstract

This paper investigated delamination failure in a unidirectional curved composite laminate. The curved laminate failed unstably by delaminations developing around the curved region of the laminate at different depths through the thickness until virtually all bending stiffness was lost. Delamination was assumed to initiate at the location of the highest radial stress in the curved region. A closed form curved beam elasticity solution and a 2-D finite-element analysis (FEA) were conducted to determine this location. The variation in the strain energy release rate, G, with delamination growth was then determined using the FEA. A strength-based failure criterion adequately predicted the interlaminar tension failure which caused initial delamination onset. Using the G analysis the delamination was predicted to extend into the arm and leg of the laminate, predominantly in mode I. As the initial delamination grew around the curved region, the maximum radial stress in the newly formed inner sublaminate increased to a level sufficient to cause a new delamination to initiate in the sublaminate with no increase in applied load. This failure progression was observed experimentally.

17. Key Words (Suggested by Author(s))	18. Distribution Statement
Composite materials Curved laminate Delamination Fracture toughness Strain energy release rate	Unclassified - Unlimited Subject Category - 39

19. Security Classif. (of this report)	20. Security Classif. (of this page)	21. No. of pages	22. Price
Unclassified	Unclassified	43	A03